

# Single cell visual proteomics through pattern mining

Min Xu<sup>1</sup>, Elitza I Tocheva<sup>4</sup>, Yi-Wei Chang<sup>2</sup>, Grant J Jensen<sup>2,3</sup>, and Frank Alber<sup>1,5</sup>

*1 Program in Molecular and Computational Biology, University of Southern California, Los Angeles, California, USA.*

*2 Division of Biology and Biological Engineering, California Institute of Technology, Pasadena, California, USA.*

*3 Howard Hughes Medical Institute, Pasadena, California, USA.*

*4 Department of Stomatology, Université de Montréal, Montreal, Quebec, CANADA.*

*5 Corresponding author*

**Cryo-electron tomography enables 3D visualization of cells in a near native state to molecular resolution. The produced cellular tomograms contain detailed information about all macromolecular complexes, their structures, their abundances and their specific spatial locations in the cell. However, extracting this information is very challenging due to image distortions, relative low resolution, and the highly crowded molecular environment. Here, we formulate the task of extracting the information as a reference-free pattern mining problem, and propose a set of novel analysis methods and integrate these methods into a software system to support proteome-scale mining of 3D structures from cellular tomograms. Our tests on simulated and experimental tomograms show that the methods are promising for visual proteomics analysis.**

Nearly every major process in a cell is orchestrated by the interplay of macromolecular assemblies, which often coordinate their actions as functional modules in biochemical pathways. In order to proceed efficiently, this interplay between different macromolecular machines often requires a distinctly nonrandom spatial organization in the cell. Therefore, when modeling complex biological functions, it is crucial to know the structure, abundance and locations of the entire set of large macromolecular complexes. Currently, proteomics studies have explored the component lists of proteins often extracted from a lysed cell population, but little is known about how proteins and their complexes are spatially arranged in an individual crowded cell at its native state, limiting the plausibility of modelling complex biological functions.

With cryo-electron tomography (ECT), it is now available to generate 3D reconstructions of cells in hydrated, close to native states at molecular resolutions. New imaging technologies and advances in automation are allowing labs to quickly obtain large numbers of cryo-electron tomograms. It is therefore now possible to undertake a “visual proteomics”<sup>1,2</sup> analysis of large macromolecular complexes in cells. However, the detection and structural analysis of unknown macromolecular complexes in tomograms remains very challenging due to a number of factors. First, macromolecular complexes can vary significantly in shape, size, and cellular abundance. Second, identifying individual complexes is significantly more difficult in cellular tomograms than in isolated samples, due to high crowding levels<sup>3</sup>. Third, individual tomograms often have low signal-to-noise ratio (SNR) and low contrast, in particular cellular tomograms, for which the sample is relatively thick (>300nm). In addition, the tomogram image is modulated by the Contrast Transfer Function (CTF) effect. Finally, the limited range of tilt angles leads to partial sampling of images and missing structural components in the Fourier space, resulting in anisotropic resolution and distortions that depend on the orientation of the object relative to the tilt axis (i.e., the missing wedge effect). Therefore, unlike large organelles, which can be detected by visual inspection, the systematic structural classification and recovery of all accessible macromolecular complexes in cellular tomograms is difficult, and can only be ventured with the aid of highly efficient automatic analysis methods.

The pioneering attempts to quantitatively analyze the spatial organizations of macromolecular complexes in cellular tomograms used “template matching”<sup>2,4</sup>. This approach uses a given complex’s known structure from other high-resolution *in vitro* methods (e.g. X-ray crystallography, NMR, cryo-EM single particle reconstruction) to simulate a ECT reconstruction,

the template, which is then used to search for matches in the experimental tomogram. Naturally, this approach is limited to detecting complexes whose 3D structures are already known, which represent only a small fraction of all the complexes in the cell. Assessing the reliability of detected matches is also challenging<sup>5</sup> because the template structure can misfit its targets, either due to conformational changes or additional bound components to the structure *in vivo*, or because the template structure is from a different organism and exhibits a different conformation<sup>6</sup>.

To overcome some of these limitations, a few template-free subtomogram averaging<sup>7</sup> and classification [e.g. <sup>8,9</sup>] approaches have been developed recently. By using iterative clustering and averaging these methods classify subtomograms into groups of similar structures. Due to the computationally intensive nature of 3D image processing (especially the subtask of subtomogram alignment), current methods are tailored to datasets usually containing a relatively small number of structural classes, for example multiple conformational or compositional states of a single macromolecular complex [e.g. <sup>8,10-12</sup>].

Thus, if we wish to apply them on a proteome-wide scale, existing template-free approaches have several drawbacks. First, the computational cost is proportional to the number of subtomograms multiplied by the number of classes. In cellular visual proteomics, the set of subtomograms will contain a large number of different complexes. Moreover, to allow for sufficient copy numbers to obtain a high SNR in each class, it is necessary to process a very large number (tens to hundreds of thousands) of subtomograms. Therefore, these applications are computationally extremely demanding<sup>13</sup>. To our knowledge, no template-free subtomogram classification method exists that is specifically optimized for and can be applied to large-scale applications in a visual proteomics setting.

Here, we propose a novel concept, *Pattern Mining*, which searches for high-quality *structural patterns* occurring frequently in a cellular tomogram. Herein, a structural pattern is defined as a set of aligned subtomograms likely to represent a single complex and its density average. We propose a new approach called *Multi Pattern Pursuit* (MPP) (Figure 1a) for pattern mining, which is specifically designed for supporting large-scale mining in visual proteomics to search for macromolecular complexes in cellular tomograms, without using templates of known structures. MPP produces the shape and abundance of the patterns as well as its position and orientation in the tomogram.

There are substantial differences between MPP and existing template-free classification methods. Our software is specifically designed to handle (i) large numbers of subtomograms extracted from cellular tomograms (tens of thousands of subtomograms); (ii) sets of subtomograms that may include a large number of different structural classes, with widely varying shapes, sizes, and abundances; and (iii) subtomograms extracted from a crowded environment<sup>3</sup>, which may include fragments of neighboring complexes as well as the target complex.

MPP is an iterative constrained optimization process that maximizes the total quality of a set of structural patterns that are distinct with respect to their average density and disjoint subtomogram membership. That is, MPP strongly discourages its patterns from sharing subtomograms. MPP generates candidate patterns from the collection of subtomograms and stores them into a growing pattern library. At each new MPP iteration, a new selection of distinct patterns is made from this library, based on the pattern quality. Specifically, we search for the best combination of patterns leading to the best overall quality score, while having a maximal coverage of the subtomograms without substantial overlap of subtomograms between the selected patterns. The corresponding density averages of the selected patterns then serve as references for updating the rigid transformations of all subtomograms, which in turn leads to newly generated candidate patterns in the following MPP iteration step. With each iteration, and therefore to a growing pattern library. To achieve this goal, MPP relies on a very efficient subtomogram alignment<sup>9</sup> algorithm based on constrained correlation and fast rotational matching<sup>14</sup>, and an efficient, robust, and flexible parallel architecture<sup>15</sup> that supports high-throughput processing. In addition, MPP contains procedures to optimize patterns by removing likely misassigned subtomograms and also procedures to remove redundant patterns from the library.

Next, we describe the main steps of the MPP method in more detail. Each MPP iteration consists of the following steps (Figure 1a, Supplementary Note 1.1.1):

**(Step 1) Candidate Pattern Generation** (Supplementary Note 1.1.3). Each MPP iteration starts by generating candidate patterns consisting of subtomograms likely to contain similar objects. At every iteration, the complete set of subtomograms is processed using their currently assigned rigid transformations (the very first iteration uses randomly assigned transformations). Note that in one iteration, multiple independent methods can be used to generate different/alternative sets of patterns, which will all be added to the pattern library. Here we use two different methods to generate patterns:

**1)** We apply k-means clustering of the subtomograms in a reduced data space. Due to the computational complexity we propose a method for dimension reduction that accounts for missing-wedge effect (Supplementary Note 1.1.3.1) and the structural heterogeneity of complexes. At early iterations a fixed cluster number  $K$  is used that is chosen to be large enough to increase the chance of detecting patterns of relatively low abundance, while being small enough so that there are sufficient numbers of subtomograms in each cluster to generate a meaningful first pattern density average. At later iterations an automatically determined value for  $K$  is used.

**2)** Patterns are also generated by a sequential expansion method (Supplementary Note 1.1.3.2), which optimizes the quality of patterns already generated in the previous iterations: for a given pattern, the subtomograms are ranked based on their alignment scores to the pattern average (obtained in MPP step 5 of the previous iteration). Then a score cutoff is searched that maximizes the quality for a newly formed pattern containing only the subset of subtomograms with alignment scores above the cutoff. This procedure allows the exclusion of likely misclassified subtomograms. (This method is applied at later iterations of the MPP optimization process).

Next, the subtomograms in all generated patterns are averaged to generate the pattern densities.

**(Step 2 and 3) Determine the quality of the pattern** (Supplementary Note 1.1.2) **and expand pattern library** (Supplementary Note 1.1.4). We quantify the quality of the density average of each pattern as a “Sum of the Fourier Shell Correlation” (SFSC) score, which takes into account missing wedge effects and can be efficiently computed. All newly generated patterns and their quality score are then added to the pattern library.

**(Step 4) Selecting disjoint set of candidate patterns of high quality from pattern library.**

A new selection of distinct candidate patterns is made from the pattern library, based on the pattern quality. Specifically, we search for the best combination of patterns leading to the best overall quality score, while having a maximal coverage of subtomograms and without substantial overlap in subtomogram membership between the selected patterns. The selected candidate patterns serve as references for subtomogram alignments in the next step.

**(Step 5) Alignment of selected patterns into common reference frames** (Supplementary Note 1.1.5). The density averages of the selected patterns are aligned into common reference frames, which reduces potential biases resulting from their translational and orientational differences in the subsequent dimension reduction step.

**(Step 6) Alignment of all subtomograms against all the selected patterns.** Next, we calculate the best alignments between each subtomogram and each of the density averages of all selected candidate patterns. For each subtomogram the transformation and alignment scores against each of the pattern density averages are stored.

**(Step 7) Redundant pattern detection and removal** (Supplementary Note 1.1.6). It is possible that two patterns, formed by disjoint sets of subtomograms, represent the same complex. The structural redundancy of two patterns is determined by a statistical test. If two patterns are structurally similar, the one with lower quality is considered redundant and removed from both the current pattern selection and the pattern library.

**(Step 8) Storing rigid transformation for each subtomogram.** Finally, the rigid transformation of each subtomogram is updated using the best of all alignments to all non-redundant selected pattern averages. These transformations are used as input information for the new pattern generation step in the next MPP iteration.

**(Optional Step 8b for crowded samples) Automatic masking of target complexes.** In a cellular tomogram, a subtomogram is often extracted from a crowded environment. Besides the target complex, a subtomogram may contain neighbor structures and regions of background noise that can substantially bias the processing. As an optional component, we introduce a method for automatic target complex segmentation.

The whole process (steps 1-8) is repeated until a new iteration does not generate any new, non-redundant candidate patterns and has therefore converged to a final set of patterns. The output are the candidate patterns of the final iteration, the subtomograms assigned to each pattern and their rigid transformations.

In addition to the core MPP framework our software also contains several optional tools that facilitate the pattern recognition in cellular tomograms (Figure 1b).

**Pre-processing steps** (Figure 1b). To further increase the efficiency of image processing, we introduce an optional pre-filtering step, which provides efficient coarse classifications using clustering. The coarse clusters provide information that can be used to exclude groups of particles of low interest. This preprocessing step is particularly useful for analysis of whole cellular tomograms. In practice, a pre-filtering procedure can efficiently reduce a collection of tens of thousands of automatically selected subtomograms to sets of a few thousand subtomograms, to be processed independently with MPP.

**Post-processing: refinement of detected patterns.** We also introduce an optional post-processing step, to improve the quality of the detected patterns by refining subtomogram membership and pattern density averages (Supplementary Note 1.3).

## Results

To assess the performance of our method, we applied it to three experimental cellular tomograms from different bacteria species, and carried out two types of studies using benchmarks of realistically simulated tomograms.

**Complexes under low crowding conditions.** First, we assessed MPP with simulated subtomograms as they would be extracted under relatively low crowding conditions such as relatively thin samples of purified macromolecular complexes or cell extracts. We applied our method to 11,230 realistically and strongly distorted subtomograms cut from a single simulated tomogram, containing a benchmark mixture of 22 different macromolecular complexes with a wide range of abundances (Supplementary Note 2.1.3). To our knowledge, this is a substantially larger number of subtomograms and structures than any previously published classification study. The benchmark set of complexes is selected to have a wide range of variation in size and abundance, as well as distinct shapes (Figure 2b).

After 32 iterations our results converged and MPP detected 12 patterns from the highly distorted subtomograms (Figure 2ab and Supplementary Data 1). In general, subtomograms of the same type of complex were highly abundant in no more than one pattern (Figure 2a). Also the detected patterns were highly homogenous with respect to subtomogram membership. All twelve patterns were enriched with one dominant complex and the shapes of all detected pattern averages were very similar to the corresponding true complexes. Eight patterns uniquely matched complexes with a false discovery rate (FDR)  $\leq 10\%$ . Among these, four patterns had an FDR of 0%, meaning that all the subtomograms in each pattern were generated from the same true class. Also, the structural consistency (in terms of FSC, with 0.5 cutoff) between the average densities of the 8 complexes and the corresponding ground truth structures is very strong: it ranges between 4.7 nm to 5.2 nm, which is comparable to the applied resolution. The best performances were achieved with the largest complexes, such as Glutamine Synthetase (2GLS) (FDR=0%, 88% of subtomograms detected), GroEL (1KP8) (FDR=0%, 75% of subtomograms detected), 50S ribosomal subunit (2AWB) (FDR=0%, 57% of subtomograms detected) and 20S Proteasome (3DY4) (FDR=0%, 48% of subtomograms detected), Carbonyl

Phosphate synthase 1BXR) (FDR=1%, 42% of subtomograms detected), RecA hexamer (FDR=6%, 35% of subtomograms detected). Three patterns had larger FDRs (21%, 30% and 45%), however in each of these patterns essentially only a single complex was falsely assigned, which had very similar shapes to the target complex at the given resolution, which explains why the overall shape of the target complex was still very well predicted.

Seven complexes were not recovered (PDB ID: 1F1B, 1GYT, 1VPX, 2H12, 2IDB, 2GHO, 1QO1). The majority of these had relatively low abundance (< 200 instances), relatively small size and possibly non-discriminative shape features. Importantly, following MPP's design strategy, the subtomograms of these complexes were *not* wrongly assigned to any pattern but simply left out, emphasizing the importance of the pattern mining approach in detecting high-quality structural patterns rather than attempting to classify all subtomograms. All our results are highly reproducible when we repeated our analysis with different random initial orientations for all the subtomograms, (Supplementary Data 2). We also repeated our analysis with different complex abundances, (Supplementary Data 3). With larger copy numbers, now two additional complexes that previously had remained undetected were very well recovered. Aminopeptidase A (1GYT: FDR=1%, 79% of subtomograms detected) and Transaldolase (1VPX: FDR=0%, 48% of subtomograms detected). Two other complexes could still not be detected even though they had substantially larger copy numbers, which indicates that their relatively small size prevented their reliable detection at the given resolution.

**Complexes under high crowding conditions.** Next, we tested MPP on realistically simulated cryo-electron tomograms of environments similar to those found in cell cytoplasm, with crowded mixtures of macromolecular complexes from the same benchmark set of 22 used in the previous experiment (Supplementary Note 2.1.4.1). The crowding level of the simulated tomogram is 15.2%, which falls into the expected range for a cell<sup>16-19</sup> (Figure 2d). We used automated 'Difference of Gaussian' particle picking<sup>20</sup> to extract subtomograms likely to contain one target complex without any given structural template (Supplementary Note 2.1.4.2). However, extracted subtomograms may also contain fragments of neighboring structures. We therefore applied our method for automatically masking target complexes during each MPP iteration (Step 8b) (Supplementary Note 1.1.7). This test case is substantially more challenging than the previous one, because errors in particle picking can influence the MPP performance. Despite these challenges, MPP detected six patterns, and four of those recovered four abundant large complexes with structural consistencies ranging from 4.3 nm to 4.8 nm and false discovery rates  $\leq 23\%$  (Figure 2cd, Supplementary Data 4, and Supplementary Note 2.1.4.3). Among these, one (50S ribosome / 2AWB) had a false discovery rate of 0%. MPP also predicted two patterns that are a mix of complexes. These two have structural consistencies  $\leq 6.5\text{nm}$  and are very similar in shape to the most abundant complex in the pattern. One of these patterns contained only two complexes (2GLS) of relatively similar shapes. The detected pattern with the smallest size is a mixture of more than 10 complexes, most of which are relatively small and similar in shape as evidenced by their tight clustering based on shape similarity when comparing all target complexes (Supplementary Figure 7). At the given resolution and crowding level it is not possible to distinguish these small complexes. However, MPP predicted their size and location. To test the reproducibility of the recovered patterns, we repeated our analysis by simulating another tomogram containing the same set of complexes with the same abundance. The results are very similar to the original test (Supplementary Data 5). We also tested MPP with simulated tomograms having the same SNR level but a lower crowding level. In this case MPP gives improved performance (Supplementary Note 2.1.4.4 and Supplementary Data 6).

**Experimental cellular tomograms.** We tested MPP on three cellular cryo-electron tomograms of bacteria, namely single cells of lysed *Acetonebma longum*, intact *Hylemonella gracilis* sample and intact *Bdellovibrio bacteriovorus* sample. We performed automated, template-free particle picking to extract a total of ~30,000 subtomograms from the three cells as described in Supplementary Notes 2.2.1, 2.2.2, and 2.2.3. For intact cells (*H. gracilis* and *B. bacteriovorus*) the cell regions are manually segmented and only the subtomograms within the cells are extracted. The cell of *A. longum* appeared lysed and particles were noticeable also at the cell exterior, which was included in the analysis. We then applied pre-filtering. We applied MPP separately for each filtered subtomogram collections.

For the three cells, MPP discovered 12, 15 and 10 patterns of relatively high quality score for *A. longum*, *H. gracilis* and *B. bacteriovorus*, respectively (Figure 3ab; Supplementary Notes 2.2.1.3, 2.2.2, and 2.2.3; Supplementary Data 7, 8 and 9; Supplementary Movies 1, 2 and 3): the Gold Standard FSC of these patterns ranged in resolution from 4.1-5.8 nm, from 3.5-10.5 nm and from 4.8-15.0 nm respectively. These ranges reflect different degrees of reproducibility for the patterns of a given cell type. The shapes and positions of some patterns already give indications as to the identity of the complexes. For example, several different patterns clearly represent membrane particles lining the cell boundaries (Figure 3ab). Other patterns are small globular complexes of various different shapes (Supplementary Data 7b, 8b and 9b). Some larger patterns have shapes and sizes very similar to the known structures of GroEL (pattern 4 in *A. longum*) and ribosomes (patterns 0, 1, 2 in *H. gracilis*; and patterns 0, 1, 9 in *B. bacteriovorus*), and were also observed at relatively large abundance.. We refined these patterns further (Supplementary Note 1.3). Figure 3c demonstrates the similarity between these structures and GroEL and 70S ribosome templates simulated from their atomic structures.

Strikingly, when we fit the atomic structure of GroEL into the average density of pattern 4 detected by MPP in *A. longum* we observe a remarkably good fit (Figure 3c). As a proof of principle, we further assessed the likelihood of GroEL complexes by several criteria, using a template-based search (Supplementary Notes 2.2.1.4, 2.2.2 and 2.2.3). Specifically, we aligned all the subtomograms from each cell type against a collection of the 28 different template structures that are most abundant in cells. We found that the alignment scores for subtomograms of the GroEL-like pattern 4 (resolution 4.5 nm, Supplementary Data 7b) were statistically significantly more similar to the GroEL template (PDB ID: 1KP8) than any other template (one-sided Wilcoxon rank-sum test with p-value  $3.2 \times 10^{-10}$ , Supplementary Figure 10a), confirming the clear visual similarity of pattern 4 to GroEL. The second closest match was the GroEL/GroES complex (PDB ID: 1AON), although this template had significantly lower alignment scores. Also, we showed that the subtomograms of pattern 4 had the strongest matches to the GroEL template, in terms of alignment scores, compared to all the rest of the extracted the 9,703 subtomograms of *A. longum* (p-value  $< 2.2 \times 10^{-220}$ ). These tests indicate that our reference-free approach yields results similar to a template matching approach, when using the GroEL structure as a template (Supplementary Figure 10b). All these observations support the hypothesis that the subtomograms in pattern 4 contain a bacterial analog of the GroEL complex. Interestingly, the high abundance of GroEL complexes (481 instances) observed only in the *A. longum* cell may be related to a stress response, as we note that this cell was lysed and appeared to be dead before image acquisition<sup>21</sup>.



Equally convincing are the assessments of ribosome structures in *H. gracilis* and *B. bacteriovorus* cells. In *H. gracilis*, three patterns (patterns 0, 1, and 2) are visually similar to known ribosome structures (Figure 3c). This observation is confirmed by template based assessment. The subtomograms in pattern 0, 1, and 2 had indeed the highest alignment scores when matched to the ribosome template (PDB ID: 2J00-2J01) (Supplementary Figure 12c) (p-value  $< 4.9 \times 10^{-35}$ ) compared to any of the other 26 templates showing that all three patterns are likely ribosome structures. The subtomograms of pattern 1 (resolution 8.7nm, Supplementary Data 8b) had the highest alignment scores (p-value  $< 1.5 \times 10^{-65}$ , Supplementary Fig. 12a) with respect to the ribosome templates (both the full ribosome PDB ID: 2J00-2J01 and its 50S subunit with PDB ID: 2AWB). Also subtomograms in pattern 0,1,2 had the highest alignment scores with the ribosome templates compared to all other extracted subtomograms (p-value  $< 2.0 \times 10^{-125}$ , Supplementary Fig. 12bc). All these observations support the hypothesis that these patterns contain a ribosome structure.

Similarly, in *B. bacteriovorus*, the subtomograms in pattern 1 (resolution 12.0 nm, Supplementary Data 9b) were visually similar to the ribosome and had significantly higher alignment scores to the ribosome templates (PDB ID: 2J00-2J01 and 50S subunit with PDB ID: 2AWB) compared to any of the other 26 templates (p-value  $< 1.8 \times 10^{-24}$ , Supplementary Figure 14a). Also, among all the detected patterns only subtomograms in pattern 1 had the highest alignment scores to the ribosome template (PDB ID: 2J00-2J01) (Supplementary Figure 14c) and also had the highest-ranking alignment scores compared to all other extracted subtomograms (p-value  $< 2.4 \times 10^{-26}$ , Supplementary Figure 14b). With similar shapes, subtomograms from patterns 0 and 9 also have relatively high alignment scores with respect to the ribosome template and are also likely to contain a ribosome analog.

Interestingly, we found distinct spatial distributions for the different complexes in the *B. bacteriovorus* tomogram. For instance, the likely ribosomal patterns are excluded from a region along the central axis of the cell (Supplementary Figure 15b), where the bacterial nucleoid is expected to be. It is likely that ribosomes would be located close to, but not directly overlapping with, regions of the genome. Ribosome-like structures also appear to be less abundant in the tip region associated with the bacterial flagella motor, although we cannot excluded imaging artefact being responsible for the lack of ribosome structures in this region. A, smaller pattern was only enriched in the tip of the bacteria (patterns 4 and 5, Supplementary Figure 15c). A different small pattern was found only in the region that may be occupied by the bacterial nucleoid genome (pattern 6) (Supplementary Figure 15d).

The purpose of this paper is to describe and make available our MPP method and software. Therefore biological interpretations of the above observations would go beyond the scope of the paper. However, the observations add examples of the potential usefulness of our method.

## Summary

In summary, our MPP method is designed to process a large number of subtomograms containing many different structural classes, in a high-throughput and template-free fashion, and derive robust structural patterns. More importantly, our method represents a substantial step towards visual proteomics analysis inside single cells. Automatic pattern mining inside cellular ECT tomograms is still very challenging. On the other hand, together with recent breakthroughs

on direct detectors<sup>22</sup> and phase plates<sup>23</sup> that significantly improve contrast and resolution of whole-cell ECT data, correlative light and electron microscopy<sup>24</sup> that specifically identify target regions of a big cell to image by ECT, focused ion beam milling<sup>25</sup> that enables ECT to image a substantially larger variety of cell types, we expect that our method can become an integral part of visual proteomics applications. In addition, MPP is also useful for analyzing tomograms containing isolated but highly heterogenic particle mixtures, such as cell lysates. Moreover, once patterns are detected in a whole cell analysis, they can be used by other methods such as template searches [e.g. <sup>2,4,5,26</sup>], subtomogram classifications [e.g. <sup>8,10,27-30</sup>] and subtomogram averaging methods [e.g. <sup>7,31</sup>] for further refinement. Therefore, our work complements existing template-based and template-free methods.

## Acknowledgements

This work was supported by NIH R01GM096089, Arnold and Mabel Beckman Foundation (BYI), NSF career to F.A..

# Figures

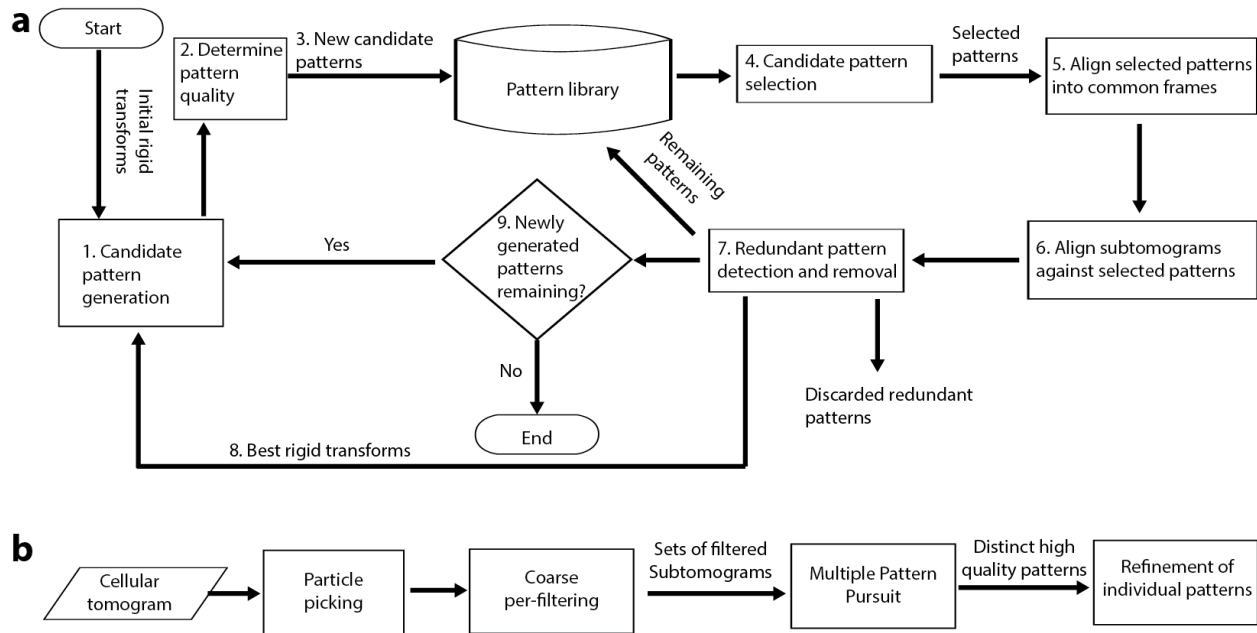


Figure 1: Overview of the method. (a) Flow chart of the MPP method (Supplementary Note 1.1.1). (b) Flow chart of overall processing pipeline, including preprocessing and postprocessing of cryo-electron tomograms. In the flow charts, actions are in boxes, data are on arrows, and diamond represents decisions.

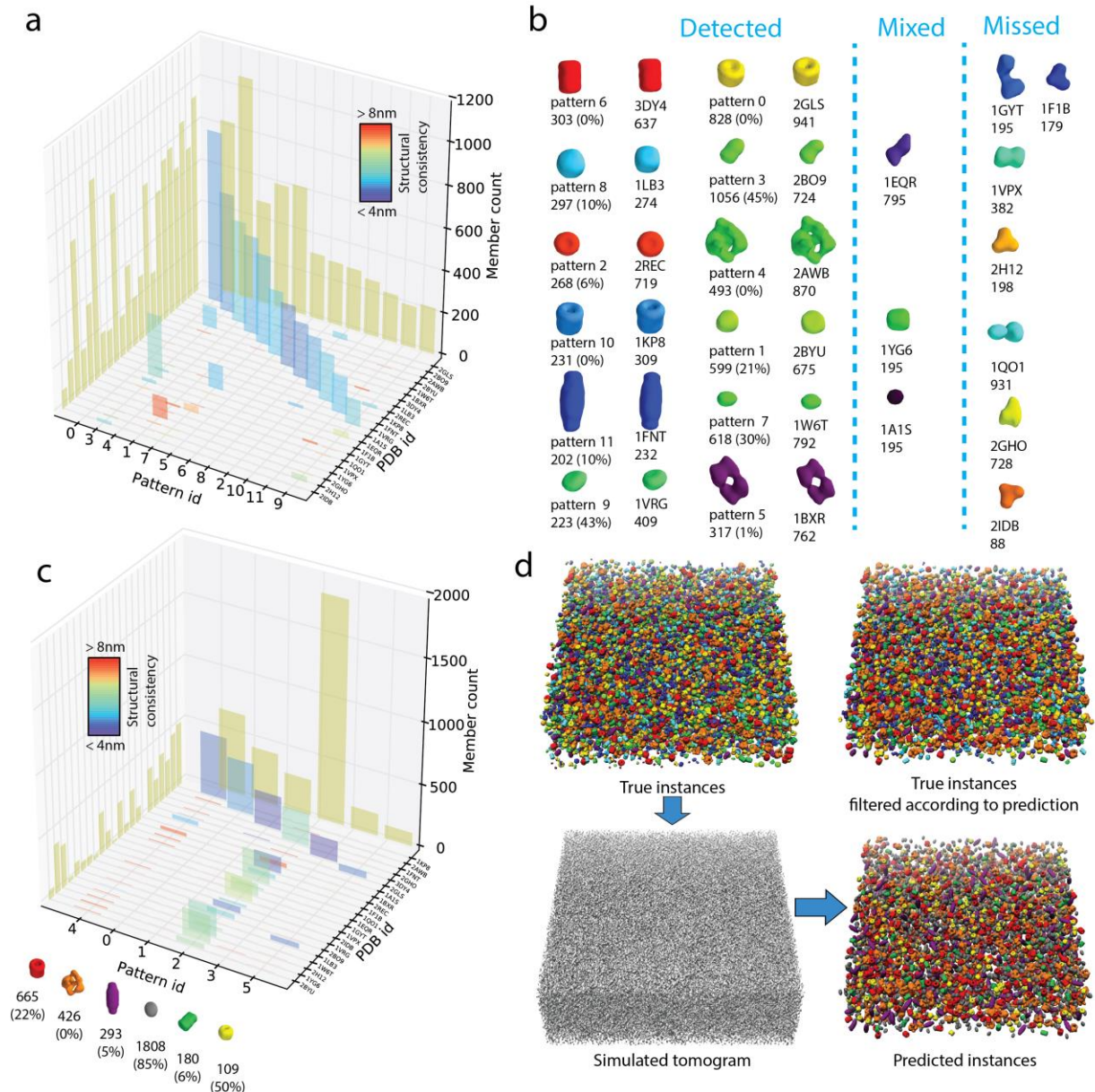


Figure 2: Comparison of MPP pattern mining results with ground truth complexes for individually simulated subtomograms and tomograms containing a crowded mixture of complexes. (a) Results of individually simulated subtomograms, column plot representation of the contingency table (Supplementary Data 1c) of the subtomogram membership overlap between true and inferred patterns. The height of each column corresponds to the number of subtomograms of the ground truth complex and the predicted patterns. The colors of the columns indicate the structural similarity between the ground truth and the corresponding pattern averages, quantified as FSC with cutoff 0.5 (Suppl. section 2.1.2). (b) The isosurfaces of predicted patterns compared to ground truth structures. The ground truth structures are indicated by their PDB ID code, and the number of instances. Also shown are the isosurface representations of the predicted patterns with the number of instances and the false discovery rate (FDR) in parentheses. The FDR shows the fraction of wrongly assigned subtomograms in the pattern. (c) Column plot representation of the contingency table for the simulated cellular tomogram of a

crowded mixture of complexes (Supplementary Data 4c). Also shown are the isosurface representations of the predicted patterns with the number of instances and FDR in parentheses. (d) Upper left panel: isosurface of the ground truth mixture of crowded complexes. Lower left panel: isosurface of the simulated tomogram. Lower right panel: isosurface representation of the predicted patterns and their localizations. Upper right panel: True instances that were detected using MPP.

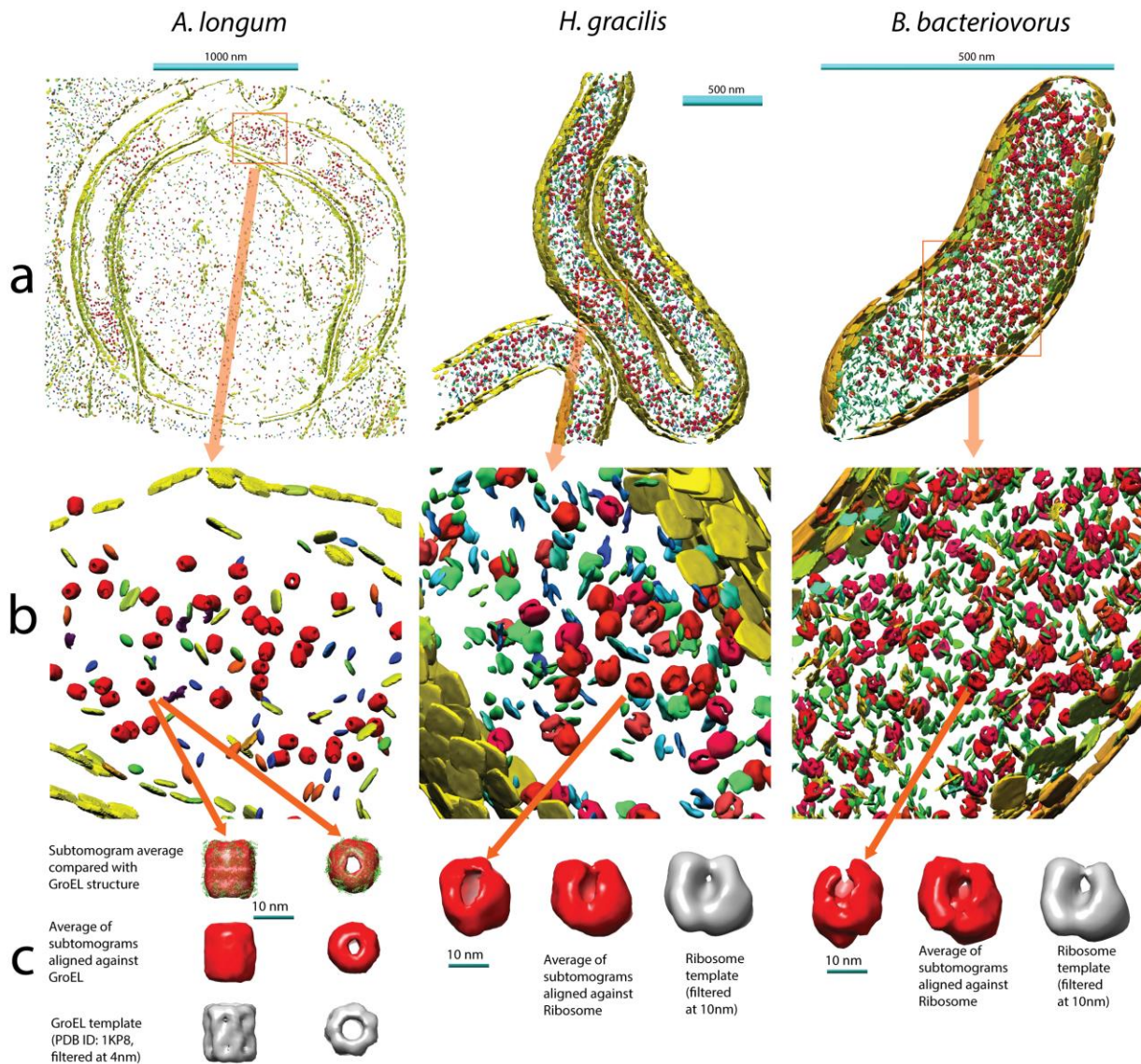


Figure 3: Discovered patterns in three cellular tomograms: *A. longum*, intact *H. gracilis*, and intact *B. bacteriovorus* cells (left, middle, right). (a) Embedded instances of patterns. (b) Embedded instances, zooming in on a particular region. (c) Isosurfaces of one example pattern from each experiment. The GroEL-like pattern is also fitted with a known atomic model of GroEL. Isosurface of the average density of the example pattern, aligned with the known structures of the GroEL and ribosome complexes.

## References

1. Nickell, S., Kofler, C., Leis, A. P. & Baumeister, W. A visual approach to proteomics. *Nat. Rev. Mol. Cell Biol.* **7**, 225–230 (2006).
2. Beck, M. *et al.* Visual proteomics of the human pathogen *Leptospira interrogans*. *Nat. Methods* **6**, 817–823 (2009).
3. Lučić, V., Rigort, A. & Baumeister, W. Cryo-electron tomography: The challenge of doing structural biology in situ. *Journal of Cell Biology* **202**, 407–419 (2013).
4. Frangakis, A. S. *et al.* Identification of macromolecular complexes in cryoelectron tomograms of phantom cells. *Proc. Natl. Acad. Sci. U. S. A.* **99**, 14153–14158 (2002).
5. Yu, Z. & Frangakis, A. S. M-free: Scoring the reference bias in sub-tomogram averaging and template matching. *J. Struct. Biol.* **187**, 10–19 (2014).
6. Han, B.-G. *et al.* Survey of large protein complexes in *D. vulgaris* reveals great structural diversity. *Proc. Natl. Acad. Sci. U. S. A.* **106**, 16580–16585 (2009).
7. Briggs, J. a G. Structural biology in situ - the potential of subtomogram averaging. *Current Opinion in Structural Biology* **23**, - (2013).
8. Bartesaghi, a. *et al.* Classification and 3D averaging with missing wedge correction in biological electron tomography. *J. Struct. Biol.* **162**, 436–450 (2008).
9. Xu, M., Beck, M. & Alber, F. High-throughput subtomogram alignment and classification by Fourier space constrained fast volumetric matching. *J. Struct. Biol.* **178**, 152–164 (2012).
10. Chen, Y., Pfeffer, S., Fernández, J. J., Sorzano, C. O. S. & Förster, F. Autofocused 3D classification of cryoelectron subtomograms. *Structure* **22**, 1528–1537 (2014).
11. Scheres, S. H. W., Melero, R., Valle, M. & Carazo, J. M. Averaging of Electron Subtomograms and Random Conical Tilt Reconstructions through Likelihood Optimization. *Structure* **17**, 1563–1572 (2009).
12. Kuybeda, O. *et al.* A collaborative framework for 3D alignment and classification of heterogeneous subvolumes in cryo-electron tomography. *J. Struct. Biol.* **181**, 116–127 (2013).
13. Asano, S., Engel, B. D. & Baumeister, W. In situ cryo-electron tomography: A post-reductionist approach to structural biology. *J. Mol. Biol.* (2015).
14. Kovacs, J. a. & Wriggers, W. Fast rotational matching. *Acta Crystallogr. Sect. D Biol. Crystallogr.* **58**, 1282–1286 (2002).
15. Frazier, Z., Xu, M. & Alber, F. TomoMiner and TomoMinerCloud: A software platform for large-scale subtomogram structural analysis. *submitted*
16. Ellis, R. J. Macromolecular crowding: An important but neglected aspect of the intracellular environment. *Current Opinion in Structural Biology* **11**, 114–119 (2001).
17. Vazquez, A. Optimal cytoplasmic density and flux balance model under macromolecular crowding effects. *J. Theor. Biol.* **264**, 356–359 (2010).
18. Guigas, G., Kalla, C. & Weiss, M. The degree of macromolecular crowding in the cytoplasm and nucleoplasm of mammalian cells is conserved. *FEBS Lett.* **581**, 5094–5098 (2007).

19. Dill, K. A., Ghosh, K. & Schmit, J. D. Inaugural Article: Physical limits of cells and proteomes. *Proceedings of the National Academy of Sciences* **108**, 17876–17882 (2011).
20. Langlois, R., Pallesen, J. & Frank, J. Reference-free particle selection enhanced with semi-supervised machine learning for cryo-electron microscopy. *J. Struct. Biol.* **175**, 353–361 (2011).
21. Susin, M. F., Baldini, R. L., Gueiros-Filho, F. & Gomes, S. L. GroES/GroEL and DnaK/DnaJ have distinct roles in stress responses and during cell cycle progression in *Caulobacter crescentus*. *J. Bacteriol.* **188**, 8044–8053 (2006).
22. Jin, L. *et al.* Applications of direct detection device in transmission electron microscopy. *J. Struct. Biol.* **161**, 352–358 (2008).
23. Murata, K. *et al.* Zernike phase contrast cryo-electron microscopy and tomography for structure determination at nanometer and subnanometer resolutions. *Structure* **18**, 903–912 (2010).
24. Chang, Y.-W. *et al.* Correlated cryogenic photoactivated localization microscopy and cryo-electron tomography. *Nat. Methods* **11**, 737–9 (2014).
25. Rigort, A. *et al.* Focused ion beam micromachining of eukaryotic cells for cryoelectron tomography. *Proc. Natl. Acad. Sci. U. S. A.* **109**, 4449–4454 (2012).
26. Xu, X.-P., Page, C. & Volkman, N. Efficient Extraction of Macromolecular Complexes from Electron Tomograms Based on Reduced Representation Templates. in *Computer Analysis of Images and Patterns* 423–431 (2015).
27. Förster, F., Pruggnaller, S., Seybert, A. & Frangakis, A. S. Classification of cryo-electron sub-tomograms using constrained correlation. *J. Struct. Biol.* **161**, 276–286 (2008).
28. Heumann, J. M., Hoenger, A. & Mastrorarde, D. N. Clustering and variance maps for cryo-electron tomography using wedge-masked differences. *J. Struct. Biol.* **175**, 288–299 (2011).
29. Yu, Z. & Frangakis, A. S. Classification of electron sub-tomograms with neural networks and its application to template-matching. *J. Struct. Biol.* **174**, 494–504 (2011).
30. Stölken, M. *et al.* Maximum likelihood based classification of electron tomographic data. *J. Struct. Biol.* **173**, 77–85 (2011).
31. Bharat, T. A. M., Russo, C. J., Löwe, J., Passmore, L. A. & Scheres, S. H. W. Advances in Single-Particle Electron Cryomicroscopy Structure Determination applied to Sub-tomogram Averaging. *Structure* (2015).